Numerical microstructural optimization for the hydrogen electrode of solid oxide cells

Manon Prioux, Eduardo da Rosa Silva, Maxime Hubert, Julien Vulliet, Johan Debayle, Peter Cloetens, Jérôme Laurencin

To cite this version:

Manon Prioux, Eduardo da Rosa Silva, Maxime Hubert, Julien Vulliet, Johan Debayle, et al.. Numerical microstructural optimization for the hydrogen electrode of solid oxide cells. Fuel Cells, 2023, 10.1002/fuce.202300029 . emse-04185252

Numerical Microstructural Optimization for the Hydrogen Electrode of Solid Oxide Cells

Manon PRIOUX[1], Eduardo DA ROSA SILVA[1], Maxime HUBERT[1*], Julien VULLIET[2], Johan DEBAYLE[3], Peter CLOETENS[4], Jérôme LAURENCIN[1]

[1] Univ. Grenoble Alpes – CEA/LITEN, 38054, Grenoble, France
[2] CEA, DAM, Le Ripault, F-37260, Monts, France
[3] CNRS, UMR 5307 LGF, Centre SPIN, MINES Saint-Etienne, Saint-Etienne, France.
[4] ESRF – The European Synchrotron, 71 Avenue des Martyrs, 38043 Grenoble, France

[*] Corresponding author: E-mail: maxime.hubert@cea.fr – Telephone: +33 (0)438784360– Fax: +33 (0)438784139

Abstract

A multiscale model has been used to optimize the microstructure of a classical hydrogen electrode made of nickel and yttria stabilized zirconia (Ni-8YSZ). For this purpose, a 3D reconstruction of a reference electrode has been obtained by X-ray nano-holotomography. Then, a large dataset of synthetic microstructures has been generated around this reference with the truncated gaussian random field method, varying the ratio Ni/8YSZ and the Ni particle size. All the synthetic microstructures have been introduced in a multiscale modeling approach to analyze the impact of the microstructure on the electrode and cell responses. The local electrode polarization resistance in the hydrogen electrode as well as the complete cell impedance spectra have been computed for the different microstructures. A significant performance improvement was found when decreasing the Ni particle size distribution. Moreover, an optimum has been identified in terms of electrode composition allowing the minimization of the cell polarization resistance. The same methodology has been also applied to assess the relevance of graded electrodes. All these results allow a better understanding of the precise role of microstructure on the cell performances and provide useful guidance for the cell manufacturing.

Keywords

Solid Oxide Cell, Electrolysis, Hydrogen Electrode, Microstructure, Modelling

1 Introduction

Because of the global warming, the massive deployment of decarbonized energies sources becomes nowadays a necessity. In this context, hydrogen can play a key role as a clean energy vector especially when produced with renewable energy sources [1]. Among the different technologies that can be considered for hydrogen production, the high-temperature electrochemical devices present a great potential and have gained remarkable interest in recent years. Indeed, the solid oxide cells (SOCs) have several advantages such as a high efficiency, a good reversibility in electrolysis mode (SOEC) or fuel cell (SOFC) mode as well as the ability to co-electrolyze steam and carbon dioxide [2-5]. Despite all the advantages, in order to be economically competitive, this technology still needs improvements regarding both the cell performances and the long-term durability. Indeed, the operating current density must be increased up to -1.5 A cm^{-2} to reach the targeted price of hydrogen while the degradation rate must be limited to ensure a lifetime of 40,000 hrs. However, the degradation rates measured upon operation are still high and constitute one of the main issues of the SOCs technology [6,7]. These degradations are associated with various phenomena activated at high temperatures like electrode microstructural evolution, electrode poisoning, materials instabilities or reactivity [8-11].

The complex electrode microstructures play a major role in the global cell performances and durability by controlling the rates of the electrochemical reactions [12-14]. Regarding the standard hydrogen electrode made of a cermet of nickel and yttria stabilized zirconia (Ni-YSZ), one of the key microstructural properties is the active triple phase boundaries lengths (TPBl) defined by the lines where the percolated ionic, electronic and gas phases meet. Indeed, the density of active TPBl are the lines in the microstructure where the electrochemical reactions take place [15-17]. In the literature, it has been shown that an increase of the active TPBl density can be obtained by decreasing the particle sizes [18-20]. Furthermore, it has been observed that a coarse cermet microstructure favors the Ni depletion under electrolysis mode while a fine microstructure allows limiting this phenomenon [21,22]. The size, quantity and connectivity of the gas phase is also essential to facilitate the gas transportation up to the reaction sites [23]. Thus, the repartition between the different phases in a composite electrode has a significant impact on the electrode efficiency and the long-term stability of the hydrogen electrode [22]. Therefore, tuning the electrode microstructure appears like a relevant strategy to design more efficient and durable SOCs.

The microstructural optimization can be conducted by manufacturing electrodes with different compositions or particle sizes. For example, Holzer et al. [24], have manufactured many electrodes by changing the particle size distribution in order to modify the TPBl density. Other experimental studies have been dedicated to optimize electrodes with graded composition [25-28]. In these cases, the number of investigated microstructure is rather limited since the manufacturing is complex and time consuming. To overcome this issue, numerical approaches have been used to identify the best electrode microstructure. Indeed, modelling offers the alternative for fast evaluation of the effect of various microstructural parameters that influence the main microstructural properties like the density of TPBl and the effective ionic/electronic conductivities. Some studies focused on the simulation of a number of synthetic microstructures and the extraction of the main microstructural properties from the produced dataset [29,30]. In these cases, the TPBl density evolution is used as a relevant indicator to identify the best electrode microstructure. To go further, other works have implemented the microstructural properties deduced from the synthetic electrodes in electrochemical models [31-33]. For example, Ni et al. [27] have used a model developed at the cell level to discuss the effect of gradients in porosity and particle size. They found that the gain in performances for micro-structurally graded electrode with respect to conventional microstructure is more pronounced for smaller electrode–electrolyte interfacial particles. They also noticed that particle size grading is generally more effective than porosity grading while the maximum power density can be increased by one-fold in comparison with homogeneous microstructure. This numerical approach facilitates the identification of the optimized electrode microstructure to reach the best current-voltage characteristics. Nevertheless, the generation of synthetic graded microstructures relevant of real electrode is not straightforward and only simplified methods have been used in the literature for the microstructural optimization.

In the present study, it is proposed to use a multiscale-modeling approach to optimize the microstructure of a hydrogen electrode made of Ni-YSZ. For this purpose, the electrochemical characteristics measured on a typical complete cell along with the 3D reconstruction of the tested electrode is used as reference for the numerical study. The multiscale model combines synthetic microstructure with electrochemical modeling tools at the electrode and cell levels. In particular, the truncated pluri-gaussian random field method has been employed to generate representative microstructures of the Ni-YSZ functional layer. With the purpose to find the best compromise for the electrode performance, different microstructures have been investigated by varying the solid volume ratio as well as the particle size in homogenous and graded electrodes.

The results are discussed and recommendations are provided for electrode design and manufacturing.

2 Experimental

2.1 Cell Description and Test Conditions

A hydrogen electrode supported cell with an active surface area of 9.08 cm² has been used for this study. The cell is composed of a thick cermet substrate of 300 µm made of NiO and zirconia stabilized with 3 mol.% of yttria (NiO-3YSZ) on which is layered a functional layer of 25 µm in NiO-8YSZ (with 56 vol.% of 8YSZ and 44 vol.% of Ni). The dense electrolyte of 8 µm, made up of 8YSZ, was co-sintered with the cermet. The oxygen electrode, deposited by screen-printing into the electrolyte, is composed of two layers: (i) an active part of 22 µm thick constituted of a LSCF-CGO composite with $La_{0.6}Sr_{0.4}Co_{0.2}Fe_{0.8}O_{3-\delta}$ (LSCF) perovskite and 20 mol.% ceria doped gadolinium oxide (CGO), and (ii) the current collector made of LSCF with a thickness of 20 µm. A thin CGO barrier layer is also added between the oxygen electrode and the electrolyte to limit the materials reactivity.

The cell has been tested in an in-house test bench following the protocol already presented in [34]. The electrochemical performances have been measured at 750 °C in fuel cell and electrolysis modes using a potentiostat/galvanostat (Autolab PGSTAT-302N) equipped with a frequency response analyzer module (FRA) and a 20 A current booster. In particular, polarization curves in electrolysis mode and electrochemical impedance spectra (EIS) at open circuit voltage (OCV) have been recorded with gas condition pH_2/pH_2O = 10/90 at the hydrogen electrode and air at the oxygen electrode. The total molar fluxes were kept constant during the entire experiment for both electrodes ($3.06\text{x}10^{-5}$ mol s^{-1} cm^{-2} and $4.47\text{x}10^{-6}$ mol s^{-1} cm^{-2} for the air and fuel electrodes, respectively).

2.2 Hydrogen Electrode Reconstruction

The initial microstructure of the cermet (Ni-8YSZ) has been characterized by X-ray holotomography at the Nano Imaging beamline ID16A of the European Synchrotron Radiation Facility (ESRF). To perform the holotomographic experiment, a micro-pillar with a diameter of 40 µm has been extracted from the hydrogen electrode using a plasma-focused ion beam (pFIB) vion (FEI) as already detailed in [14,21]. The specimen has been characterized using a specific protocol adapted to the SOC materials [35]. With this technique, a large representative volume of $50 \text{ x } 25^2 \text{ x } \pi$ μm^3 has been reconstructed with a voxel size of 25 nm. The region of interest containing the functional layer of the hydrogen electrode and a part of the dense electrolyte has been cropped in the reconstruction for the microstructural analysis. The different phases have been segmented in the volume using a set of numerical tools already presented in [36,37]. The main microstructural properties such as the density of active TPBl, the volume fraction of each phase (ε_x), the specific surface areas (S_p) and the mean phases diameters have been calculated for the initial electrode.

2.3 Model Description

2.3.1 Synthetic Microstructure Generation

For the sensitivity analysis on the microstructure, a mathematical method based on the gaussian random fields method [38,39] was used to produce synthetic electrode, with the studied Ni-YSZ cermet taken as reference. The model description and its validation for classical electrode composed of three phases (i.e. two solid phases and the porosity) are detailed in [40]. Therefore, only the main characteristics of the method are reminded hereafter as well as the adaptation to simulate graded electrode microstructures. In practice, this method consist in the generation of a random gaussian noise, which is then correlated with a weight function. This function includes the geostatistical information related to the emulated stochastic microstructure. It should be noticed that for a three phases electrode, two independent fields (associated to the Ni and YSZ for instance) are generated before being combined into a bi-Gaussian field that follows a normal bivariate distribution. The fields are then thresholded to obtain a synthetic volume with the same average properties than the targeted microstructure. The ability to reproduce microstructures well representative of SOCs electrodes has been validated in previous works [40]. Indeed, the comparison with real reconstructed microstructures has shown error limited to a few percent. Another advantage of this method is its fast execution time compared to the more classical sphere packing algorithms [41-43] since the process does not require iterations. For example, the generation of a 600 x 600 x 600 voxels^3 microstructure representative of a three phase electrode took only 230 s with a workstation using two CPU Intel$^©$ Xenon$^©$ Gold with 28 cores each.

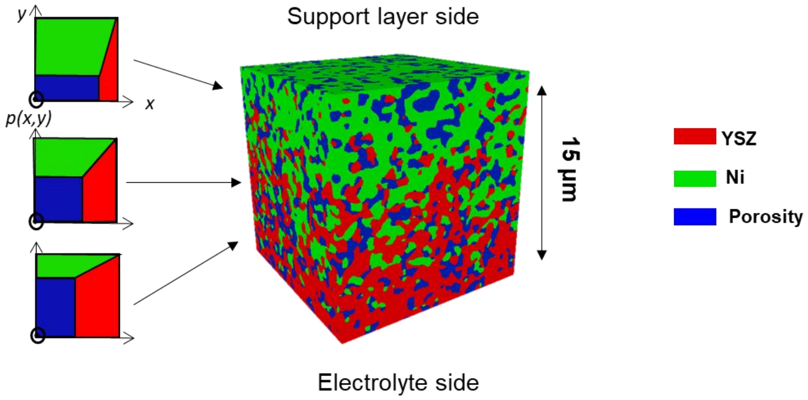

Fig. 1. Graded electrode simulated with the local thresholding [40].

The flexibility of the random field model allows investigating specific architectures such as graded electrode in composition [40]. It requires introducing a spatially dependent threshold for the phase segmentation. In the case of the hydrogen electrode, the ionic and electronic conducting phases should exhibit a continuous and opposite gradient while the porosity is kept constant in the electrode. This result is obtained by changing the threshold value for the bivariate distribution along the electrode thickness. The partitioning of the phases has been optimized to obtain relevant specific surface area with a microstructure showing a gradient. The evolution of the domain partitioning in the electrode is shown in Figure 1 as well as the resulting graded microstructure. This model offers a large flexibility to investigate different design of the hydrogen electrode.

2.3.2 Multi-Scale Modelling Approach

A multi-scale electrochemical model has been developed in order to analyze the impact of the operating mechanisms and material properties on the cell efficiency. This numerical tool is especially relevant to unravel the complex relationships between the reaction mechanisms occurring in the electrodes and their microstructural properties. The model has been already thoroughly detailed in [34] and is briefly described hereafter. At the macroscopic scale, a two-dimensional model takes into account the gas flow configuration and describes the distribution of local gas compositions, overpotentials and current density along the cell length. The electrode functional layers are not explicitly described and the electrochemical reactions are assumed to occur in the vicinity of the electrode/electrolyte interface. The activation overpotentials are computed using microscale elementary kinetic models developed for each electrode. At this scale, a 1D slice of the active layer is simulated using the gas partial pressures and current density computed at the macroscopic level as boundary conditions. The elementary model for the oxygen electrode made of LSCF-CGO is detailed in [19]. For the Ni-8YSZ hydrogen electrode model, the complex reaction mechanism considered in the numerical approach is widely described in [44]. The model is based on a hydrogen spillover mechanism taking into account gas interactions with both Ni and YSZ surfaces. It is worth noting that the microstructural properties of the reference cell for both electrodes and the Ni-3YSZ support have been used as input data in the simulations for a thorough model validation already reported in [44]. In the present work, the model has been used to compute the cell polarization curve and the impedance spectra at OCV as well as the local electrode polarization in the hydrogen electrode.

3 Results and Discussions

3.1 Microstructural Characterization and Model Validation

As shown in Figure 2a for the functional layer of the cermet, the segmented volume presents a size of 15 x 15 x 15 µm^3 (= 3,375 µm^3). It is worth noting that a volume of 12 x 12 x 12 µm^3 is sufficient to be well representative of a typical cermet electrode microstructure [40]. Therefore, since the size of the analyzed volume can be considered as statistically representative of the studied Ni-8YSZ electrode microstructure, it was used to determine the main microstructural properties with a good level of confidence.

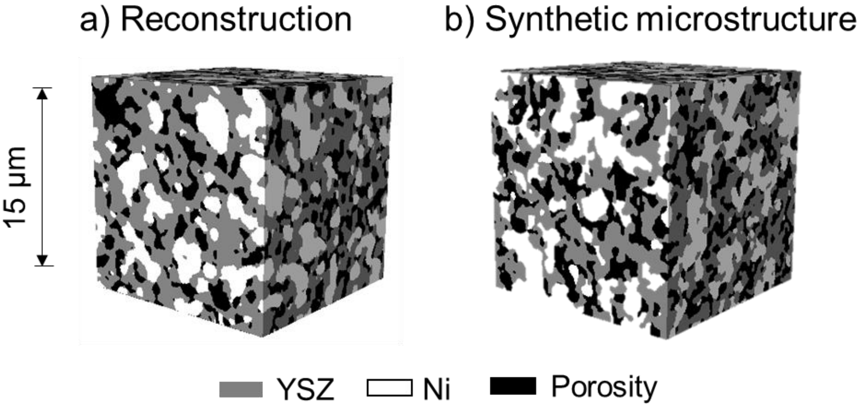

Fig. 2. 3D rendering volumes for (a) the real cermet electrode and (b) its corresponding synthetic microstructure emulated with the Gaussian random field method.

The 3D rendering volume reveals a quite homogeneous and fine microstructure. To confirm the observations, the main microstructural properties have been extracted from the reconstruction and are given in Table 1. Regarding the volume fraction, it can be noted that the ratio between the Ni and 8YSZ solid phases is consistent with the one used for the electrode manufacturing. Indeed, the volume fractions of solid phases measured on the reconstruction correspond to a cermet made of 56 vol.% of 8YSZ and 44 vol.% of Ni which is in perfect agreement with the electrode manufacturing (cf. section 2.1). This result allows validating the correct segmentation of the 3D reconstruction. For all the phases, it is has been found that the connectivity remains higher than 98% meaning that the percolation is good in all of them. The mean phase diameters are also provided in Table I. It can be observed that the gas and 8YSZ phases are fine while the Ni particles exhibit a quite large mean diameter. These coarse particles result in a low Ni specific surface area and a relatively low density of active TPBl (3.14 µm^{-2}). Nevertheless, most of the microstructure reported in the literature exhibit TPBl values in a relatively narrow range between 1 and 4 µm^{-2} [45]; the microstructure studied here is included in this area. Finally, it can be noticed that the gas and Ni phases exhibits rather high tortuosity factors.

Table 1: Microstructural properties of the tested Ni-8YSZ functional layer taken as reference and relative error between real and synthetic microstructures.

	Real microstructure			Relative error between real and synthetic microstructure		
Properties	Porosity	YSZ	Ni	Porosity	YSZ	Ni
Volume fraction / %	24	42	34	0%	-2%	2%
Specific surface area / µm^{-1}	1.89	2.59	1.45	7%	-11%	-5%
Active TPBl density / µm^{-2}		3.14			-17%	
Tortuosity factor / -	5.33	2.45	6.61	-9%	1%	-54%
Mean phase diameter / µm	0.25	0.35	0.57	-4%	-1%	-9%

A digital twin of the real functional layer has been emulated with the Gaussian random field method. As it can be observed on the 3D rendering of Figure 2b, the simulated Ni-8YSZ electrode seems to reproduce accurately the complex microstructure, showing the capability of this approach to mimic SOCs electrodes. The effective representativeness of the synthetic microstructure has been verified by comparing the properties extracted from the 3D volume with those from the reference electrode (Table 1). As it can be noted, a general good agreement has been obtained between the parameters of the real and synthetic microstructures. Indeed, the relative errors on the predicted microstructural properties with respect to the real ones are limited to a few percent except for the tortuosity factor of the Nickel phase. In this case, the discrepancy between the two microstructures can be explained by the high value obtained for the real electrode [40]. Nevertheless, it can be claimed that the errors remain acceptable so that the model can be considered as validated to generate representative synthetic microstructures of the studied hydrogen electrode.

Taking the properties of the emulated synthetic microstructure together with all the input data already provided in [34] for the same type of cells, the multiscale model has been used to simulate the polarization curve and EIS diagram specifically measured for the present study (cf. experimental conditions reported in section 1.1). The comparison between the experimental and the simulated data is shown in Figure 3 at 750 °C, pH_2/pH_2O = 10/90. It can be seen that the shape of the impedance in the Nyquist and Bode plots as well as the *I-V* curve are rather well reproduced by the model. Three main contributions appears in the impedance spectra as can be observed in Figure 3b. Thanks to the simulation, it is possible to ascribe these contributions to a process. The one arising at low frequency is due to the gas conversion at the hydrogen side. The second and third contributions at intermediate and high frequencies are mainly related to the electrochemical processes in the active layer of the oxygen and hydrogen electrodes, respectively.

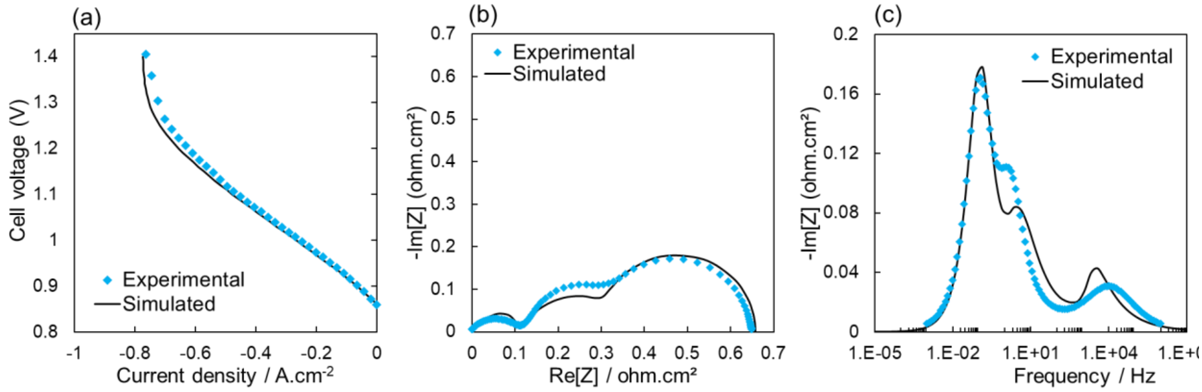

Fig. 3. (a) Experimental and simulated polarization curves and (b-c) impedance spectra at OCV for the complete cell : (b) Nyquist (c) Bode plots, at 750°C, $p(H_2O)/p(H_2)=90/10$ with a total flux of 4.47 10^{-6} mol.s^{-1}.cm^{-2} at the hydrogen side.

3.2 Generation of Synthetic Microstructures for the Ni-8YSZ Electrode

To better understand the role of cermet microstructure on the electrode performances, a large dataset of synthetic microstructures has been generated around the reference case (i.e. the reconstructed cermet shown in Figure 2). In particular, the ratio of 8YSZ and Ni defined as $^{\varepsilon_{YSZ}}/_{\varepsilon_{YSZ}+\varepsilon_{Ni}}$ has been changed from 10% to 90% while keeping a constant porosity at 24%

in the electrode. Moreover, the Ni mean particle size being relatively large in the reference electrode (d_{Ni} = 0.52 µm), the generation of microstructures with a smaller Ni particle diameter (d_{Ni} = 0.35 µm) has been also performed to complement the sensitivity analysis. As an illustration, some 3D rendering of synthetic microstructures generated for the study are shown in Figure 4.

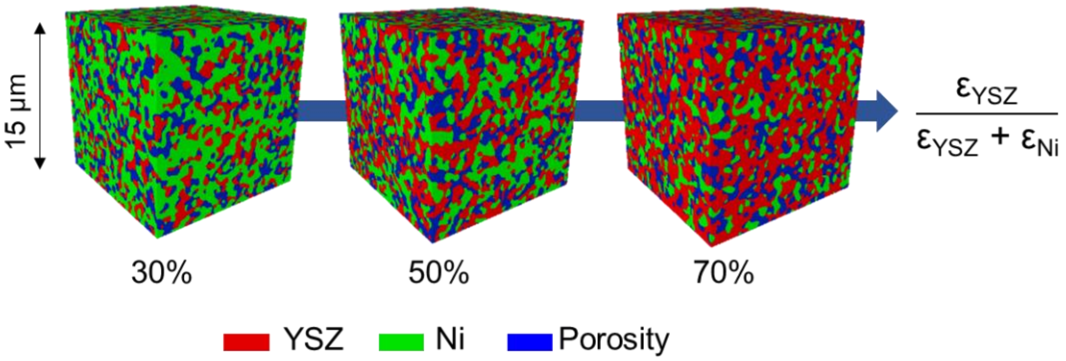

Fig. 4. Illustration of some synthetic microstructures emulated with the Gaussian random field method using a Ni mean particle = 0.35µm, a porosity of 24% for different cermet composition.

For the sensitivity analysis, all the microstructural properties have been computed from the generated synthetic microstructure and plotted as a function of the electrode composition for the two investigated Ni particle size. The evolutions for the YSZ-pore and Ni-pore specific surface areas, the *M* factor (ratio between the effective and bulk conductivities), and the density of active TPBl are shown in Figure 5. As expected, all these properties are found to be strongly dependant on the 8YSZ/Ni ratio.

As already discussed in [19,46,47], the curve for the density of active TPBl exhibits a ‘bell’ shape with a maximum value reached when the volume fractions of YSZ and Ni in the solid phase are equivalent (Figure 5a). Furthermore, a sharp evolution occurs around 15% and 85% of YSZ volume fraction, corresponding roughly to the 8YSZ and Ni percolation thresholds in the microstructure. Indeed, below these thresholds, either the Ni or the YSZ conductivity in the composite becomes very low due to the loss of connectivity. As expected, the 8YSZ effective conductivity decreases with decreasing the 8YSZ content and becomes nil below the percolation threshold. The opposite evolution is found for the Ni effective conductivity (Figure 5c). A similar behaviour is observed for the interfacial specific surface area (Figure 5b). Indeed, the specific surface area between YSZ and pores increases continuously with increasing the

YSZ content in the solid phase. On the contrary, the Ni/Gas specific surface area decreases with increasing the YSZ percentage. Both evolutions are in good agreement with the microstructural correlations given in [19,46,47]. Finally, it can be observed that the decrease of the Ni particle size from 0.52 µm to 0.35 µm allows increasing both the density of active TPBl and the Ni/pore specific surface area, which is in good agreement with the literature [18,19,48]. This dependency is explained by the distribution of fine Ni in the whole volume. All these evolutions should have a strong impact on the cell performances.

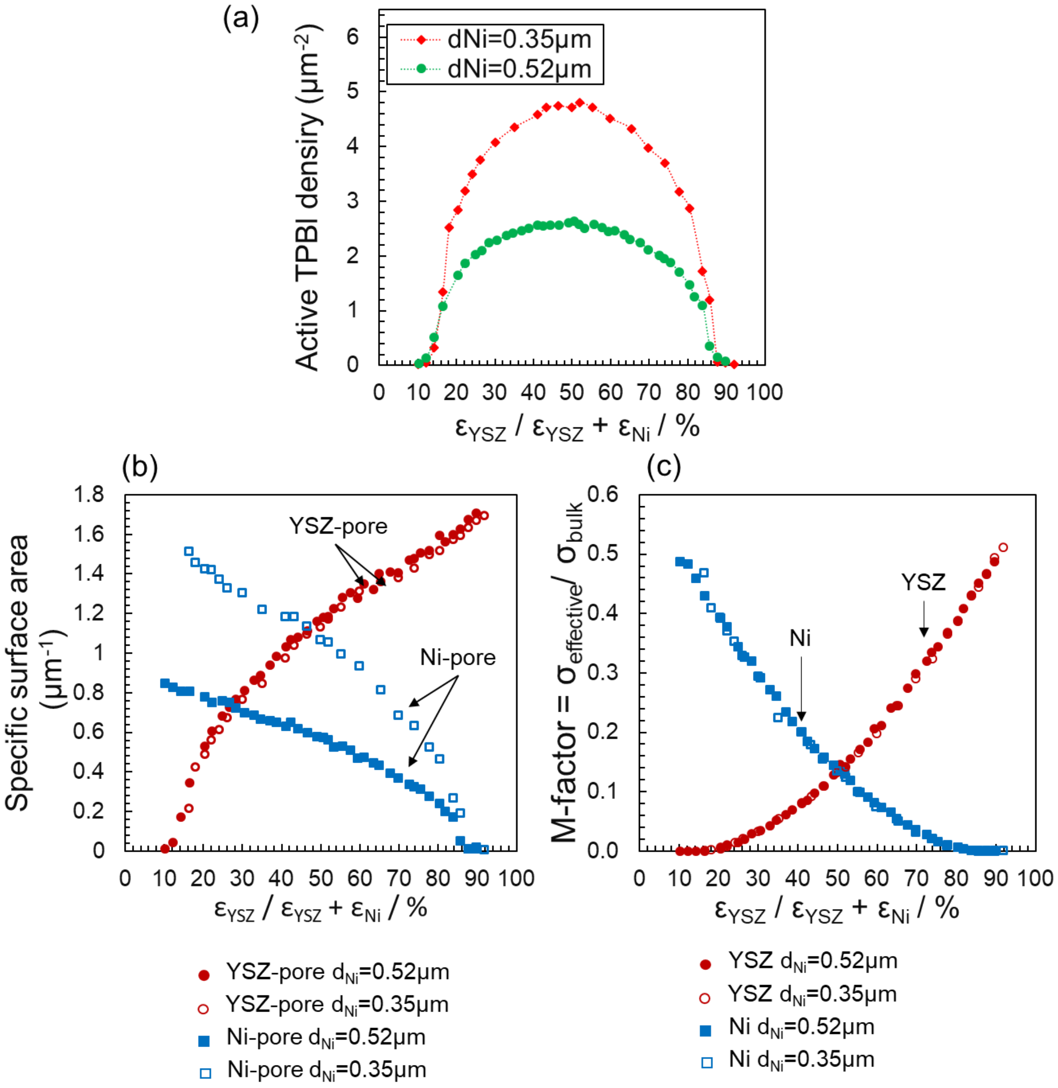

Fig. 5. Evolution of (a) active TPBl density, (b) Ni-pore and YSZ-pore specific surface area and (c) YSZ and Ni M-factors as a function of the volume fraction of YSZ in the solid phase for the two sets of microstructure (d_{Ni}=0.35 µm and d_{Ni}=0.52 µm).

3.3 Effect of the Solid Phase Ratio and the Ni Particle Size on Performances

The microstructural evolution reported in Figure 5 have been implemented in the electrochemical model to simulate impedance spectra at 700 °C and 750 °C (for the OCV, H_2/H_2O ratio:10/90, with a total flux of $4.47\text{x}10^{-6}$ mol s^{-1} cm^{-2} at the hydrogen side). The electrode polarization resistances have been taken from the simulated spectra and plotted as a function of the electrode composition in Figure 6, for the two investigated Ni particle sizes at 750 °C and 700 °C.

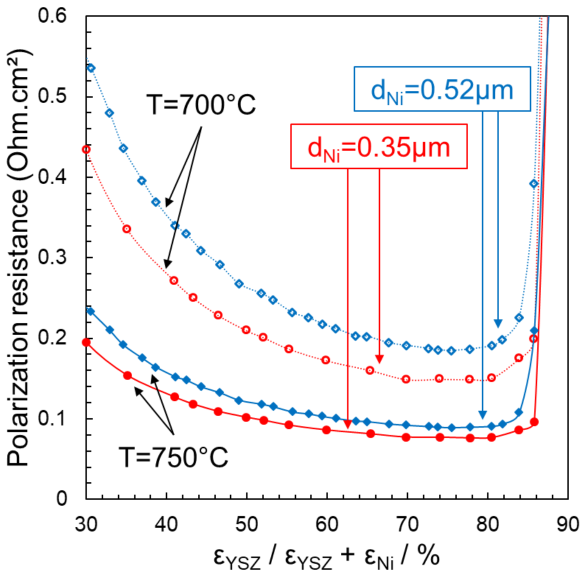

Fig. 6. Polarization resistance of the H_2 electrode as a function of the YSZ volume fraction in the solid phase for the two sets of microstructure (d_{Ni}=0.35 µm and d_{Ni}=0.52 µm) calculated at 700°C and 750°C (spectra computed at OCV, H_2/H_2O ratio:10/90, with a total flux of 4.47 10^{-6} mol.s^{-1}.cm^{-2} at the hydrogen side).

The global shape of these plots exhibits a reverse behaviour compared to the dependency of the active TPBl density with the 8YSZ content in the solid phase (cf. Figure 5a). This result can be explained since the TPBl are the electrochemical active sites for the charge transfer in the hydrogen electrode [44]. Nevertheless, it is worth mentioning that the minimum of the polarization resistance is not found for a composition of 8YSZ:Ni=50/50 vol.% that corresponds to the maximum of TPBl density. The optimum is actually shifted to around 8YSZ:Ni=70/30 vol.% regardless of the Ni particle size. Indeed, even if some active sites are lost, the increase of 8YSZ content above 50% improves the effective ionic conductivity, that leads to better performances.

From this point of view, the best compromise between optimizing the density of TPBl and the YSZ ionic conduction is identified around 65-70 vol.% of 8YSZ in the solid fraction. In addition, as shown in Figure 6, the polarization resistance decreases when the nickel particles size is decreased whatever the composition of the electrode. This statement can be explained by the increase of the active TPBl density when the electronic conducting phase is refined (cf. Figure 5a). Thus, the performance of the electrode can be considerably improved by decreasing the average particle size of Ni.

To go further in the analysis, the simulated electrochemical impedance spectra at the electrode and complete cell levels are compared in Figure 7 for the reference and the optimized microstructures.

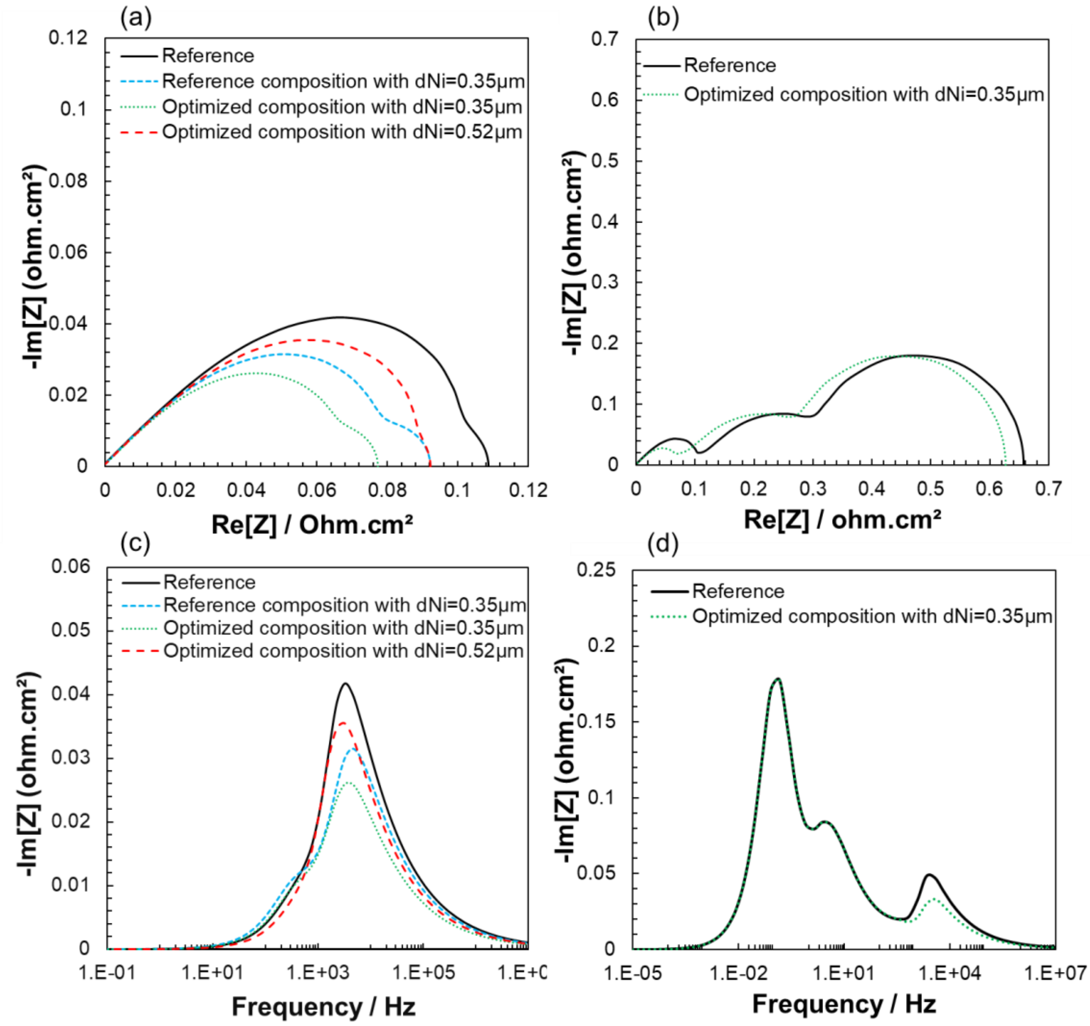

Fig. 7. Simulated impedance spectra for (a-c) the hydrogen electrode and (b-d) the complete cell at 750°C for the reference and optimized microstructures (OCV, H_2/H_2O ratio:10/90, with a total flux of 4.47 10^{-6} mol.s^{-1}.cm^{-2}).

The simulated nyquist plots at 750 °C and $p(H_2O)/p(H_2)$=90/10 are shown on Figure 7a for the H_2 electrode. In these conditions, reducing the nickel particle size from 0.52 µm (reference) to

0.35 µm or increasing the amount of 8YSZ content from 56 vol.% (reference) to 70% leads to similar performances enhancement, the gain being around 20% for both scenarios. When the optimization for both the solid phase composition and the Ni particle size are combined, a significant improvement of around 29% is found for the H_2 electrode polarization resistance (R_p = 0.108 ohm cm² *vs* 0.077 ohm cm²). Furthermore, it can be observed that the diagrams for the electrode is consistent with a kind of classical gerischer element, which has been already highlighted in the literature for typical cermets [45], convoluted with a small semicircle arising at low frequency (Figure 7a). Thanks to the model, it has been shown that the gerischer-type element is ascribed to the charge transfer at TPBl combined with the oxygen transport in 8YSZ whereas the low frequencies contribution is associated to the gas interactions with 8YSZ and Ni. As expected, reducing the Ni particle size has mainly allowed reducing the first contribution at high frequency by increasing the density of TPBl. Conversely, when the 8YSZ content is increased in the solid phase, the second contribution at low frequency is decreased due to the higher specific surface area.

The complete cell impedance spectra simulated at OCV, 750 °C and $p(H_2O)/p(H_2)$=90/10 for the reference and optimized microstructures are shown in Figure 7b. In this case, the microstructural optimization of the hydrogen electrode leads to decrease the cell polarization resistance of only 5% (R_p= 0.658 ohm cm² *vs* 0.626 ohm cm²). This statement is explained by the rather minor contribution of the H_2 electrode in the whole cell impedance spectrum at 750 °C. Nevertheless, since the charge transfer at the TPBl is strongly thermally activated, the present microstructural optimization should have a higher impact at lower temperature.

To check the relevance of this assertion, the electrode impedance spectra have been simulated at 700 °C for all the investigated microstructures. As shown in Figure 6, the dependency of the polarization resistance with the solid phase ratio is very similar for the two temperatures. It means that the optimum identified at 750 °C remains valid at 700 °C. Moreover, as expected, the polarization resistance of the electrode is higher at 700 °C than the one calculated at 750 °C for a same microstructure. It is especially interesting to note that the difference between the reference and optimized microstructure is greater at 700 °C. Indeed, the microstructural optimization allows an improvement of the hydrogen electrode performance of 36% at 700 °C, while the gain reaches only 29% at 750 °C. For the complete cell impedance spectra, the microstructural optimization of the hydrogen electrode leads to a decrease of the polarization resistance of 10%. Therefore, the optimization of the cermet microstructure is especially relevant for a low operating temperature (below 750 °C).

3.4 Effect of Graded Microstructure on Performances

The graded microstructures of the Ni-8YSZ cermet has been investigated in order to evaluate if the performances could be enhanced compared to the homogeneous microstructures. Synthetic electrodes showing different gradients have been emulated with the random field method (Table 2). For all the cases, the porosity has been kept constant in the whole electrode with a volume fraction of about 24%. The mean particle size diameter of the two solid phases has been chosen at 0.35 µm. The gradient for the ionic conducting phase has been introduced in the model assuming a linear decrease of 8YSZ volume fraction from the electrolyte interface up to the top of the functional layer. On the other hand, the electronic conducting phase present an opposite evolution with a low Ni content close to the electrolyte and higher volume fraction at the top of the layer. For both phase, the volume fraction has not been lowered below a threshold of 20% to avoid any percolation loss of the ionic or electronic network. The performances of these graded electrodes are compared in this section to the homogenous microstructures corresponding to the reference and the optimized composition by keeping a Ni particle size of 0.35 µm and a porosity of 24% (Table 2).

The YSZ/Ni ratio of the studied gradients at each side of the layer as well as their mean compositions are listed in Table 2. The first gradient has a global composition, which is almost the same than the reference electrode. The second graded microstructure has a composition at the electrolyte interface which is equal to the optimized one. In this case, the 8YSZ fraction decreases slowly from the electrolyte interface to reach a ratio of YSZ/Ni=50/50 at the top of the functional layer. The graded microstructures n°3 and n°4 have a mean composition chosen close to the optimized homogeneous electrode. In both cases, the YSZ/Ni ratio at the electrolyte interface was taken at 80/20 to promote as much as possible the effective ionic conductivity while keeping a reasonable density of active TPBl. It can be noted that the fourth gradient is slightly higher than the third one. The evolutions of the microstructural properties along the cell thickness have been computed using a slice-by-slice approach as detailed in [16]. These profiles have been then introduced in the elementary kinetic model to compute the electrochemical response of the electrode.

Table 2: Composition of the studied graded and homogeneous microstructures (d_{Ni}=0.35 µm and porosity=24%).

	YSZ/Ni volume fractions in the solid phase / vol.%		Mean composition / vol.%		
	Electrolyte side	Support side	Porosity	YSZ	Ni
Reference composition without gradient	55/45	55/45	24.9	41.3	33.5
Optimized composition without gradients	70/30	70/30	23.7	54.2	22.1
Gradient 1	65/35	45/55	23.8	42.3	33.6
Gradient 2	70/30	50/50	23.5	47.8	28.4
Gradient 3	80/20	50/50	23.4	48.7	27.4
Gradient 4	80/20	60/40	23.3	53.4	22.7

The impedance spectra of the graded hydrogen electrodes have been simulated at OCV, 750 °C in the same conditions than the previous optimization ($p(H_2O)/p(H_2)$=90/10, total inlet flux of 4.47x10^{-6} mol s^{-1} cm^{-2}). In Figure 8, the nyquist and bode plots are compared to the ones obtained with the reference and optimized homogeneous electrodes (i.e. without gradient).

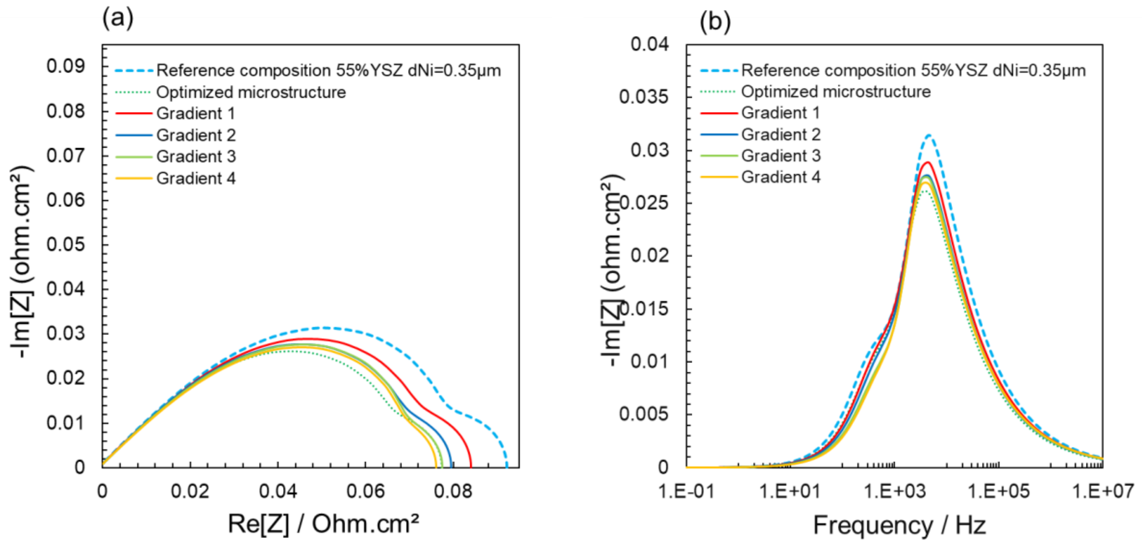

Fig. 8. Simulated impedance spectra for the hydrogen electrode at 750°C, H_2/H_2O ratio: 10/90, inlet fluxes of 4.47 10^{-6} mol.s^{-1}.cm^{-2}, for the reference composition with dNi =0.35 µm, the optimized homogeneous microstructure (dNi =0.35 µm) and the graded ones (dNi =0.35 µm) : (a) Nyquist and (b) Bode plots.

At first sight, it can be observed that the application of the selected gradients allows reducing the polarization resistance compared to the reference electrode. For instance, considering the gradient n°1 with a mean composition equivalent to the reference one, the electrode performance is clearly enhanced. Indeed, the polarization resistance is significantly decreased from 0.092 Ohm cm^2 to 0.084 Ohm cm^2 for the graded electrode n°1. It is worth noting that, as the Ni particle size and the porosity are the same for both microstructures, the density of active TPBl is also similar for both cases (i.e. 5.05 μm^{-2} *vs* 4.75 μm^{-2}). In this condition, the improvement in the electrode performance can only be attributed to the gradient.

For the other graded electrodes, the mean 8YSZ content in the solid phase has been always increased compared to the reference one up to reach for gradient n°4 the same mean composition than the optimized homogeneous microstructure. As expected, the performances are continuously increased when increasing the YSZ content from gradient n°2 to gradient n°4. However, it is worth noting that only the gradient n°4 allows reaching a slight improvement of the electrode efficiency compared to the optimized microstructure (R_p = 0.076 ohm cm^2 *vs* 0.077 ohm cm^2). In other words, the gain in performances is rather negligible when the gradient is applied on an optimized homogenous microstructure. Indeed, in this case, the higher effective ionic conductivity at the electrolyte interface for the graded electrode is entirely counterbalanced by the loss of active TPBs in this region. This result is consistent with the statement proposed by Schneider et al. [31]. Indeed, they found that the graded electrodes with varying composition did not perform significantly better than the homogeneous electrode (even if the percolation of the ionic phase is improved).

All these computations tend to confirm that the graded electrode does not allow achieving significantly improved electrochemical performances. Nevertheless, the gradient may still constitute an interesting alternative regarding the SOC reliability. Indeed, even if the performances are quite similar, the graded electrode should limit at the interface the mismatch in thermal expansion coefficients between the electrode and the electrolyte. In this way, the graded electrode would be a solution to reach a better mechanical robustness while keeping high electrochemical performances.

4. Conclusion

A coupled experimental and modeling method was used to investigate the role of the microstructure for a Ni-8YSZ cermet used as hydrogen electrode in SOCs. The overall approach combines electrochemical testing, microstructural characterization by X-ray holotomography and an in-house multi-scale modeling. A first numerical tool allows the generation of synthetic representative microstructure using the truncated gaussian random field method. In the present study, a large dataset of synthetic microstructures related to the Ni-8YSZ hydrogen electrode has been produced to perform a sensitivity analysis on relevant microstructural properties. In particular, the role of solid phase composition and the Ni particle size has been investigated for homogenous and graded electrodes. All the microstructural properties have been extracted from the synthetic 3D volumes and implemented in an electrochemical multiscale model. The cell polarization curve and the impedance spectra at OCV for both the hydrogen electrode and the complete cell have been computed for the investigated cases at 700 °C and 750 °C.

The simulations have shown that the density of active TPBl and the effective ionic conductivity of the 8YSZ backbone mainly control the electrode performances. A composition for the solid phase of about 8YSZ:Ni=(65-70):(35-30) vol.% has been identified as an optimum to enhance the electrode polarization resistance. It has been also confirmed that the size of the Ni particle has a huge impact on the performances. For instance, the polarisation resistance was significantly lowered by decreasing the mean Ni particle size from 0.52 µm to 0.35 µm. Moreover, it has been shown that the optimisation is especially relevant for an operation at intermediate temperature (700 °C) for which the contribution of the hydrogen electrode to the cell polarization resistance becomes substantial. In this condition, the fine microstructure identified in this work should also help to mitigate the Ni migration by reducing the electrode overpotentials. Finally, only a slight improvement has been found with the graded microstructures compared to the homogeneous ones. Nevertheless, electrodes with gradients could be still a relevant solution to mitigate the risk of mechanical degradation by reducing the mismatch in thermal expansion coefficient between the electrode and the electrolyte. All these statements constitute a set of guidelines to improve the efficiency of the hydrogen electrode. In future studies, the optimizations performed in this work could be refined by taking into account the mechanical robustness and the electrode stability upon operation.

Acknowledgements

This project has received funding from the Fuel Cells and hydrogen 2 Joint Undertaking (JU) under grand agreement n°874577 (NewSOC project). This work was also supported by the project CELCER-EHT, grant agreement ANR-PEHY-008, France 2030 and CASSIOPEE project. The authors also thank Genvia company for their participation.

List of Symbols

d_{Ni}	Mean phase diameter of Ni / µm
ε_X	Phase volume fraction for the phase X / -
M	Microstructure-factor / -
$p(H_2)$	Hydrogen partial pressure / atm
$p(H_2O)$	Water partial pressure / atm
R_p	Polarization resistance / Ω m^2
S_p	Specific surface area / m^{-1}
σ_{eff}	Effective conductivity of the phase X / S m^{-1}
σ_{bulk}	bulk conductivity of the phase X / S m^{-1}

References:

[1] E. L. V. Eriksson and E. MacA. Gray, *Appl. Energy* **2017**,202, 348.

[2] Q. Cai, C. S. Adjiman, N. P. Brandon, *J. Power Sources* **2014**, 268, 212.

[3] S.C. Singhal, K. Kendall, *High Temperature Solid Oxide Fuel Cells, Fundamental, Design and Applications,* Elsevier, **2003**, pp 1**.**

[4] A. Godula-Jopek, *Hydrogen Production by Electrolysis*, Wiley, **2015**, pp 191.

[5] C. Graves, S.D. Ebbesen, S.H. Jensen, S.B. Simonsen, M.B. Mogensen, *Nat. Mater*. **2015**,14, 239.

[6] M. Hubert, J. Laurencin, P. Cloetes, B. Morel, D. Montinaro, F. Lefebvre-Joud, *J. Power Sources* **2018**, 397, 240.

[7] T.L. Skafte, J. Hjelm, P. Blennow, and C.R. Graves, *Proc. 12th European SOFC and SOEC Forum*, (European Fuel Cell Forum), Lucerne, Switzerland, **2016**, pp. 8.

[8] S. Uhlenbruck, T. Moskalewicz, N. Jordan, H.-J. Penkalla, H. P Buchkremer, *Solid State Ionics* **2009**, 180, 418.

[9] H. Yokokawa, N. Sakai, T. Kawada, M. Dokiya, *Solid State Ionics* **1992**, 52, 43.

[10] H. Yokokawa, H. Tu, B. Iwanschitz, A. Mai, *J. Power Sources* **2008**, 182, 400.

[11] P. Moçoteguy, A. Brisse, *Int. J. Hydrogen Energy* **2013**, 38, 15887.

[12] E. Lay-Grindler, J. Laurencin, G. Delette, J. Aicart, M. Petitjean, L. Dessemond, *Int. J. Hydrogen Energy* **2013**, 38, 6917.

[13] A. Bertei, B. Nucci, C. Nicolella, *Chem. Eng. Sci.* **2013**, 101, 175.

[14] M. Hubert, J. Laurencin, P. Cloetens, J.C. da Silva, F. Lefebvre-Joud, P. Bleuet, A. Nakajo, E. Siebert, *Solid State Ionics* **2016**, 294, 90.

[15] J. Hanna, W.Y. Lee, Y. Shi, A.F. Ghoniem, *Progress in Energy and Combustion Science*, **2014**, 40, 74.

[16] DG. Goodwin, H. Zhu, AM. Colclasure, RJ. Kee, *J. Electrochem. Soc*. **2009**, 156, 1004.

[17] A. Bieberle, LP. Meier, LJ. Gauckler, *J Electrochem Soc* **2001**, 148, 646.

[18] Q. Cai, CS. Adjiman, NP. Brandon, *Electrochimica Acta* **2011**, 56, 5804.

[19] E. Effori, H. Moussaoui, F. Monaco, R.K. Sharma, J. Debayle, Y. Gavet, G. Delette, G. Si Larbi, E. Siebert, J. Vulliet, L. Dessemond, J. Laurencin, *Fuel Cells* **2019**,19, 429.

[20] L. Mastropasqua, A. Donazzi, S. Campanari, *Fuel Cells* **2019**, 2, 125.

[21] F. Monaco,M. Hubert, J. Vulliet, J.P. Ouweltjes, D.Montinaro, P. Cloetens, P. Piccardo, F. Lefebvre-Joud, J. Laurencin, *J. Electrochem. Soc.* **2019**, 166, 1229.

[22] A. Hauch, K. Brodersen, F. Karas, M. Chen, *Solid State Ionics* **2016**, 293, 27.

[23] M. Poon, O. Kesler, *J. Power Sources* **2012**, 210, 204.

[24] L. Holzer, B. Iwanschitz, Th. Hocker, B. Münch, M. Prestat, D. Wiedenmann, U. Vogt, P. Holtappels, J. Sfeir, A. Mai, Th. Graule, *J. Power Sources* **2011**, 196, 1279.

[25] J. Kong, K. Sun, D. Zhou, N. Zhang, J. Mu, J. Qiao, J *J. Power Sources* **2007**, 166, 337.

[26] A.C. Muller, D. Herbstritt, E. Ivers-Tiffée, *Solid State Ionics* **2002**, 152, 537.

[27] L. Nie, Q. Sun, Z. Liu, M. Liu, *International Journal of Hydrogen Energy* **2015**, 40, 16503.

[28] J. McCoppin, I. Barney, S. Mukhopadhyay, R. Miller, T. Reitz, D. Young, *J. Power Sources* **2012**, 215, 160.

[29] D. Chen, Z. Lin, H. Zhu, R.J. Kee, *J. Power Sources* **2009**, 191, 240.

[30] B. Timurkutluk, Y. Ciflik, T. Altan, O. Genc, *Int. J. Hydrogen Energy* **2022**, 73, 31446.

[31] L.C.R. Schneider, C.L. Martin, Y. Bultel, L. Dessemond, D. Bouvard, *Electrochim. Acta* **2007**, 52, 3190.

[32] M. Ni, M. K.H. Leung, D. Y.C. Leung, *J. Power Sources* **2007**, 168, 369.

[33] Z. Yan, A. He, S. Hara, N. Shikazono, *Energy Conversion and Management* **2019**, 198, 111916.

[34] E. Da Rosa Silva, G. Sassone, M. Prioux, M. Hubert, B. Morel, J. Laurencin, *J. Power Sources* **2023**, 556, 232499.

[35] M. Hubert, A. Pacureanu, C. Guilloud, Y. Yang, J.C. da Silva, J. Laurencin, F. Lefebvre-Joud, P. Cloetens, *Appl. Phys. Lett*. **2018**, 112, 203704.

[36] F. Usseglio-Viretta, J. Laurencin, G. Delette, J. Villanova, P. Cloetens, D. Leguillon, *J. Power Sources* **2014**, 256, 394.

[37] J. Villanova, J. Laurencin, P. Cloetens, P. Bleuet, G. Delette, H. Suhonen, F. Usseglio-Viretta, *J. Power Sources* **2013**, 243, 841.

[38] B. Abdallah, F. Willot, D. Jeulin, *J. Microsc.* **2016**, 263, 51.

[39] C. Lantuéjoul, *Geostatical Simulation: Model and Algorithms*, Springer, **2002**.

[40] H. Moussaoui, J. Laurencin, Y. Gavet, G. Delette, M. Hubert, P. Cloetes, T. Le Bihan, J. Debayle, *Comput. Mater. Sci.* **2018**, 143, 262.

[41] B.S. Prakash, S.S. Kumar, S.T. Aruna, *Renew. Sustain. Ener. Rev*. **2014**, 36, 149.

[42] Y. Nishida, S. Itoh, *Electrochimica Acta* **2011**, 56, 2792.

[43] H. Moussaoui, J. Debayle, Y. Gavet, P. Cloetens, J. Laurencin, *Powder Technology* **2020**, 367, 67.

[44] F. Monaco, E. Effori, M. Hubert, E. Siebert, G. Geneste, B. Morel, E. Djurado, D. Montinaro, J. Laurencin, *Electrochimica Acta* **2021**, 389, 138765.

[45] O. M. Pecho, A. Mai, B. Münch, T. Hocker, R.J. Flatt, L. Holzer, *Materials* **2015**, 8, 7129.

[46] A.M. Gokhale, S. Zhang, M. Liu, *J. Power Sources* **2009**, 194, 303.

[47] H. Moussaoui, R.K. Sharma, J. Debayle, Y. Gavet, G. Delette, J. Laurencin, *J. Power Sources* **2019**, 412, 736.

[48] J.R. Wilson, J.S. Cronin, S.A. Barnett, *Scr Mater* **2011**, 65, 67.